

Quantum-Inspired Reinforcement Learning for Low-Latency Intrusion Detection in V2X and Internet-of-Vehicles Networks

Sajid Anwer^a, Rohan Farooq^b, Anwar Shah^{b,*} and Tallha Akram^a

^aDepartment of Software Engineering, College of Computer Engineering and Sciences, Prince Sattam Bin Abdulaziz University, Saudi Arabia

^bDepartment of Computer Science, National University of Computer and Emerging Sciences, Pakistan

ARTICLE INFO

Keywords:

Smart Cities
Internet of Vehicles (IoV)
Cyber Defense
Reinforcement Learning
Quantum Computing

ABSTRACT

Smart cities increasingly depend on dense edge, IoT, and vehicular networks to deliver critical urban services, including traffic control, connected mobility, infrastructure monitoring, and energy management. In this ecosystem, the Internet of Vehicles (IoV) is central to intelligent transportation, enabling continuous communication among vehicles, roadside infrastructure, and cloud-edge platforms. This connectivity, however, also enlarges the attack surface and exposes smart city and vehicular systems to evolving cyber threats that can compromise safety, privacy, data integrity, and service continuity. Conventional static defenses are often inadequate because they cannot autonomously adapt to changing attack behaviors or multi-stage intrusion patterns. This paper proposes QIRL, a Quantum-Inspired Reinforcement Learning framework built on a lightweight Deep Q-Network architecture for next-generation autonomous cyber defense. QIRL combines amplitude-phase quantum state encoding, rotation-gate-based exploration, and quantum interference reward augmentation within a cost-sensitive Markov Decision Process formulation. It further addresses class imbalance through training-only SMOTE balancing and asymmetric cost-sensitive reward shaping, while sequential MDP modeling captures temporal dependencies in multi-stage attack campaigns. The framework is evaluated on CICIDS2017 and UNSW-NB15. QIRL achieves accuracies of 97.89% and 91.04%, F1-scores of 95.22% and 91.66%, AUC-ROC values of 0.9945 and 0.9713, and True Skill Statistics of 0.9443 and 0.8244, respectively. It also attains ultra-low inference latencies of 32.5 and 45.7 microseconds per sample, corresponding to 67.77 times and 51.77 times speedups over ensemble baselines. These results show that QIRL offers a lightweight, latency-aware, and adaptive defense for smart city and IoV infrastructures.

1. Introduction

Smart cities represent a new paradigm of urban management. They integrate a diverse network of IoT and edge devices to optimize critical services. These include traffic control, energy systems, and public safety infrastructure. The Internet of Vehicles extends this ecosystem through intelligent and connected transportation systems. Unlike static smart city infrastructure, vehicular networks introduce unique vulnerabilities. These are stemming from high node mobility, heterogeneous communication protocols, and ephemeral network topologies. These factors change as vehicles traverse different coverage zones. More critically, any defensive response in autonomous vehicle systems must operate within sub-millisecond safety windows. Since this delayed threat detection directly translates to physical harm through compromised braking, steering, and collision avoidance systems.

However, these dense and highly interconnected environments expose a wide attack surface to sophisticated cyber threats. These threats include Distributed Denial of Service, injection, and reconnaissance. Furthermore, they face multi-stage attack campaigns that evolve dynamically over time. Traditional static defense systems are designed around fixed signatures and rule-based detection. Fundamentally, they cannot adapt to this evolving threat landscape. This limitation leaves critical autonomous vehicle safety systems and smart city infrastructure vulnerable to coordinated and context-aware attacks. Addressing this requires a defense mechanism that is simultaneously accurate, adaptive, and real-time capable. Additionally, it must be deployable on resource-constrained edge hardware. To date, this is a combination that no existing solution has yet achieved.

Author emails: Sajid Anwer, s.anwer@psau.edu.sa; Rohan Farooq, rohan.farooq@nu.edu.pk; Tallha Akram, t.akram@psau.edu.sa.

*Corresponding author

✉ anwar.shah@nu.edu.pk (A. Shah)

ORCID(s):

arXiv:2606.07804v1 [cs.CR] 5 Jun 2026

Existing intrusion detection research has progressed through three broad directions, each advancing capability while introducing new limitations. Early machine learning based approaches applied classical algorithms to network traffic classification with promising results. Injadat et al. [13] proposed a multi-stage ML framework with information gain feature selection achieving 99.00% accuracy, while Alshammari et al. [5] applied KNN and SVM to CAN bus data achieving 93% and 96% accuracy respectively, and Zhang et al. [28] combined genetic algorithms with Deep Belief Networks on NSL-KDD achieving 98% accuracy. Although these methods demonstrated strong classification performance, they rely on static decision boundaries that cannot adapt to evolving attack distributions, and their inference latency typically exceeds the sub-millisecond safety threshold required for autonomous vehicle deployment [22, 12]. Furthermore, deep learning approaches have addressed this limitation by learning hierarchical representations directly from raw traffic data. Nie et al. [20] proposed a CNN-based IDS for intelligent IoV roadside units, achieving an accuracy of 97.60%, Kang and Kang [15] developed a Deep Neural Network for in-vehicle CAN security, reporting 97.80%. In another study, Ashraf et al. [7] proposed an LSTM autoencoder for intelligent transportation system anomaly detection, achieving an accuracy of 98–99% on Car-Hacking by learning temporal patterns of normal traffic. Despite improved accuracy, deep learning models treat each packet as an independent observation, ignoring temporal correlations of multi-stage attack campaigns, and their inference cost grows with model depth, making real-time edge deployment increasingly challenging [9, 16].

Reinforcement learning approaches emerged to address the adaptivity gap of static classifiers by enabling agents to learn detection policies through interaction with the environment. In a formal model, Nguyen and Reddi [19] represent network intrusion detection as a sequence of decisions. By using deep reinforcement learning, they show that systems change their behavior when threats evolve. And for anomaly detection in 6G networks, Zhang et al. [27] proposed federated learning that is fair, which shows that systems learn while they are online. However current methods for intrusion detection that use reinforcement learning are not fast when they reach a stable state because the rewards are infrequent. As a result those methods do not function well when the feature spaces have many dimensions [12, 22].

Ensemble methods currently represent the state of the art in detection accuracy, with Ullah et al. [23] achieving 99.74% and 100% on CICIDS2017 and UNSW-NB15, respectively. However, ensemble classifiers composed of multiple decision trees require each input sample to traverse all constituent models for prediction, making inference computationally intensive and fundamentally incompatible with the sub-millisecond safety threshold mandated for autonomous braking and steering interventions [22, 14, 12], a critical limitation that raw accuracy metrics alone do not reveal.

Static supervised classifiers treat each network packet as an independent observation, ignoring the temporal correlations that characterize real-world multi-stage attack campaigns. Furthermore, standard loss functions fail to account for the asymmetric misclassification costs arising from the severely imbalanced traffic distributions encountered in IoV environments. Reinforcement learning approaches have shown potential in adaptive intrusion detection but remain slow to converge and limited by reward sparsity in high-dimensional feature spaces. To date, no documented approach simultaneously satisfies competitive detection accuracy and sub-millisecond inference latency on standardized IoV datasets, a dual constraint that defines the central gap this work addresses.

In this work, we propose QIRL, a Quantum-Inspired Reinforcement Learning framework. QIRL jointly resolves the accuracy-latency trade-off within a single unified architecture. By embedding quantum-inspired state encoding, interference-based training stabilization, and cost-sensitive reward augmentation into a lightweight Deep Q-Network, QIRL achieves competitive detection accuracy. It maintains sub-50-microsecond inference latency, suitable for real-time deployment on resource-constrained autonomous-vehicle edge hardware.

The main contributions of this work are as follows.

- First, we propose a novel QIRL framework that combines quantum-inspired state encoding, exploration, and reward augmentation within a lightweight DQN architecture. It achieves a sub-50 microsecond inference latency suitable for edge deployment in autonomous vehicle systems.
- Second, we introduce a Quantum Interference Module that augments the Bellman target with cosine similarity between consecutive latent state representations. Stabilizing training without adding any trainable parameters or inference overhead.
- Third, we propose a cost-sensitive asymmetric reward formulation combined with training-only SMOTE balancing. Covering severe class imbalance without data leakage, addressing a methodological flaw present in prior work.

- Fourth, we conduct a comprehensive experimental evaluation on CICIDS2017 and UNSW-NB15. Under a rigorous preprocessing protocol, demonstrating detection accuracies of 97.89% and 91.04%, AUC-ROC of 0.9945 and 0.9713, and speedups of 67.77 times and 51.77 times over ensemble baselines.
- Fifth, we develop a framework for interpretability that is structured to use SHAP feature attribution together with geometric visualization based on PCA and t-SNE. It is the first instance where someone evaluates the explainability of a reinforcement learning policy for intrusion detection in IoV environments in a systematic way. Confirming that the learned decision boundaries reflect semantically meaningful traffic structure rather than dataset artifacts.

The remainder of this paper is organized as follows. In Section 2, the authors summarize previous research that uses traditional and modern methods for intrusion detection. To define the scope of the study, Sections 3 and 4 describe the problem, the threat model and the areas where an IoV is vulnerable to attack. For a technical explanation, Sections 5 and 6 discuss the details of the QIRL framework. In Section 7, the results from experiments are provided, and Section 8 concludes the paper with directions for future work.

2. Literature Review

This section reviews existing research on intrusion detection in IoV and smart city environments, covering three progressively developed directions: traditional ML-based IDS, deep learning approaches, and reinforcement learning methods. This progression motivates the need for the adaptive, latency-aware framework proposed in this work.

2.1. Machine Learning Based Intrusion Detection

In the early stages of Intrusion Detection System research, authors used classical machine learning (ML) algorithms on network traffic data. To improve results, Injadat et al. [13] created a multi stage machine learning framework. This system uses information gain (IG) for the selection of features and includes oversampling. It is successful because it reaches a 99.00% detection rate. By doing this the researchers showed that the engineering of features and the balancing of classes are necessary steps during the preprocessing stage. For another study, Alshammari et al. [5] used K-Nearest Neighbors (KNN) besides Support Vector Machines (SVM) on Controller Area Network (CAN) bus data. Those methods are effective as they reach 93 % and 96 % accuracy but the authors did not provide data about the time the systems take to process information [18]. And Zhang et al. [28] used a genetic algorithm with a Deep Belief Network (DBN) to detect attacks on Internet of Things devices using the NSL-KDD dataset. Their method is accurate at a level of 98 %. To detect threats in autonomous vehicles, Alheeti and McDonald-Maier [4] combined back propagation neural networks with fuzzy sets. On the KDD99 dataset, they reached a rate of 97.99 %. While those ML methods are good at the task of classification, they are based on decision boundaries that do not change. Because of this lack of change, they are unable to adjust when the patterns of attacks evolve. If the systems are used, the time required for them to make a decision is usually more than the sub millisecond threshold that is necessary for safety in the Internet of Vehicles [23].

2.2. Deep Learning Based Intrusion Detection

Deep learning improved upon classical ML by learning hierarchical representations from raw traffic. Nie et al. [20] proposed a CNN-based IDS for intelligent IoV roadside units, achieving 97.60% by detecting abnormal link load patterns. Kang and Kang [15] developed a DNN for in-vehicle CAN security using probability-based packet feature vectors, reporting 97.80%. Ashraf et al. [7] proposed an LSTM autoencoder for ITS anomaly detection, achieving 98–99% on Car-Hacking by learning temporal patterns of normal traffic. Lokman et al. [17] developed stacked sparse autoencoders for unsupervised CAN outlier detection, achieving 98% F1 score. Recent hybrid DL systems have demonstrated improved IoT security: Wahab et al. [25] proposed an SDN-based cognitive IDS, and Wahab et al. [24] introduced a three-way neural network for explainable IoT intrusion detection. Ahmad et al. [2] surveyed converging security paradigms including blockchain and digital twin-based defense frameworks. Despite improved accuracy, DL models treat each packet as an independent observation, ignoring the temporal correlations of multi-stage attack campaigns. Their inference cost also grows with model depth, making real-time edge deployment challenging [21, 11].

2.3. Reinforcement Learning and Adaptive Cyber Defense

Reinforcement learning addresses the adaptivity gap of static classifiers by enabling agents to learn detection policies through environment interaction. Nguyen and Reddi [19] formally modelled network intrusion detection

as a sequential decision problem and demonstrated that DRL enables adaptive behavior under evolving threats. Al-Fuqaha et al. [3] surveyed AI methods for IoV and identified RL as a promising direction for dynamic trust management and intrusion mitigation in vehicular networks. Zhang et al. [27] proposed a fair federated learning model for 6G network anomaly detection, demonstrating adaptive online learning. Ahmad et al. [1] demonstrate that a system learns to correct errors from malicious data injections in graph neural networks when it adjusts policies. By this result, the researchers indicate that defense mechanisms are useful when they change over time, but current methods for intrusion detection that use reinforcement learning encounter difficulties [26, 29]. As an example, the learning process is slow because the feedback signals are infrequent. In addition, those systems fail to function when the data contains many different variables. On that account, the size of the feature space limits the technology. To date, no documented study shows that the systems process data in under 0.001 seconds. Because of this delay, the speed is not fast enough for the safety standards of cars that drive themselves.

2.4. Ensemble Methods

Ensemble methods currently achieve the highest reported accuracies. Ullah et al. [23] proposed a hybrid stacking ensemble combining XGBoost, Random Forest, Decision Tree, and Gradient Boosting with IG feature selection, achieving 99.75% and 100%. However, the 100% result applies SMOTE globally before splitting a data leakage condition and evaluates only a binary two-class. Under identical single-sample CPU conditions, their ensemble incurs 2,248 μ s per flow, exceeding the autonomous vehicle safety threshold of 1 ms by more than 2 \times . The survey in Table 6 confirms that no prior approach simultaneously satisfies competitive detection accuracy *and* sub-millisecond inference latency on standardised IoV datasets. This dual constraint, together with the inability of static classifiers to adapt to evolving threats, motivates the proposed QIRL framework.

3. Problem Formulation

As the Internet of Vehicles (IoV) grows quickly, the number of ways that attackers can target vehicular networks increases. On that account autonomous systems are at risk from complex cyber attacks. These malicious activities include Distributed Denial of Service (DDoS), injection and reconnaissance attacks. In Fig. 1, it is shown that current IDS solutions have a basic problem that is not but fixed. On one hand traditional ML ensemble methods like Random Forest besides Decision Trees are accurate when they detect threats. However these methods are slow because the time they take to process data is more than $\tau_{ens} > 2$ ms/flow. To ensure safe autonomous braking and steering systems must act in less than $\tau_{safe} < 1$ ms. While alternative methods are small and fast but not strong enough to identify threats in a way that is dependable. Formally, given network traffic represented as a sequence of feature vectors $X = \{x_1, x_2, \dots, x_T\}$ where each $x_t \in \mathbb{R}^d$ corresponds to a packet flow with d feature dimensions, the objective of any IDS is to learn a mapping $f_\theta : X \rightarrow Y$ where $Y = \{0, 1\}$ denotes benign and attack classes respectively. Three structural gaps in current methodology prevent this objective from being met under real-world IoV deployment constraints. First, no existing approach simultaneously satisfies the dual objective of minimizing inference latency τ while maintaining detection robustness above an acceptable threshold δ :

$$\min_{\theta} \tau(f_\theta) \quad \text{subject to} \quad \text{TSS}(f_\theta) \geq \delta \quad (1)$$

where θ represents the model parameters and TSS denotes the True Skill Statistic. Second, IoV datasets exhibit complex and asymmetric class imbalance. Standard loss functions bias the classifier toward whichever class dominates, systematically elevating either the False Negative Rate on attack-minority datasets or the False Positive Rate on attack-majority datasets:

$$\text{FNR} = \frac{1}{N} \sum_{t=1}^N \mathbf{1}[f_\theta(x_t) = 0, y_t = 1] \quad (2)$$

This demands a dataset-aware cost-sensitive formulation with asymmetric penalties applied alongside training-only SMOTE balancing to prevent data leakage:

$$J(\theta) = \frac{1}{N} \sum_{t=1}^N C(f_\theta(x_t), y_t) \quad (3)$$

In this context $C(\cdot)$ is a cost matrix that follows the rule $C(0, 1) > C(1, 0) > C(0, 0) = C(1, 1) = 0$. By using those values, the system applies the largest numerical penalty to False Negatives, which are attacks that the system does not detect. To account for False Positives, the matrix applies a smaller numerical penalty when the system disrupts traffic that is not harmful. For instances where the classification is correct, the cost is zero. And as a third point, supervised learning methods process each packet x_t as an independent data point. They ignore the temporal correlation between consecutive flows:

$$\text{Corr}(x_t, x_{t+1}) = \frac{\text{Cov}(x_t, x_{t+1})}{\sigma_{x_t} \sigma_{x_{t+1}}} \neq 0 \quad (4)$$

There is a non zero correlation in actual attack campaigns that occur in multiple stages over time. Capturing this structure requires a Markov Decision Process (MDP) formulation with state transition $P(s_{t+1} | s_t, a_t)$, enabling the agent to maximize the cumulative discounted reward:

$$G_t = \sum_{k=0}^{\infty} \gamma^k r_{t+k} \quad (5)$$

where $\gamma \in [0, 1]$ is the discount factor and r_{t+k} is the reward at step $t + k$, rather than optimizing for greedy single-step accuracy. To address all three gaps within one system, we propose QIRL: a Quantum Inspired Reinforcement Learning architecture. It uses the cost function $J(\theta)$ from Eq. 3 as a reward signal with specific weights. By using those weights, the system manages situations where some categories of data are more frequent than others. As a second step we define the process of detection as a Markov Decision Process. This choice is made to represent how events relate to each other over time as shown in Eq. 4. To improve the speed of the process, we use a small module based on quantum interference. Because of this module, the policy reaches the goals for time limits defined in eq. 1 more quickly. When the system operates, the time required for a single decision is less than one millisecond. And the system remains as correct as other methods when it identifies threats in Internet of Vehicles settings, even if the settings have unequal amounts of data.

4. Threat Model

Effective cyber defense requires formally bounding the adversary capabilities and attack surface before any defense mechanism is evaluated. We define the adversary A . Five parameters define A

$$A = (K, O, G, P, T) \quad (6)$$

In this equation K describes how much information the adversary has about the network topology. It is represented by O if the observation mode is passive sniffing or active probing. For the attack goal, G indicates if the objective is disruption, exfiltration or hijacking. There is a probability $P \in [0, 1]$ that the attack continues across time steps t . And T specifies when the attack occurs over the sequence $\{t_1, t_2, \dots, t_n\}$.

The IoV attack surface is distributed across four layers: Vehicle-to-Infrastructure (V2I), Vehicle-to-Vehicle (V2V), edge computing nodes, and cloud backend. For each layer i , let V_i denote the set of exploitable vulnerabilities. The total attack surface is then:

$$S = \sum_{i=1}^4 |V_i| \quad (7)$$

For any attack $\alpha \in V_i$, the adversary succeeds when the IDS produces a False Negative, i.e., the detection function $f(x_t) = 0$ when the true label $y_t = 1$. The False Negative Rate across N samples is:

$$\text{FNR} = \frac{1}{N} \sum_{t=1}^N \mathbf{1}[f(x_t) = 0 \wedge y_t = 1] \quad (8)$$

The framework operates under a black-box assumption: the adversary observes traffic flows x_t but cannot access or modify the reward signal r_t or learned policy parameters θ during inference. Physical layer attacks (e.g., GPS spoofing)

The Latency-Accuracy Trade-off in IoV Security

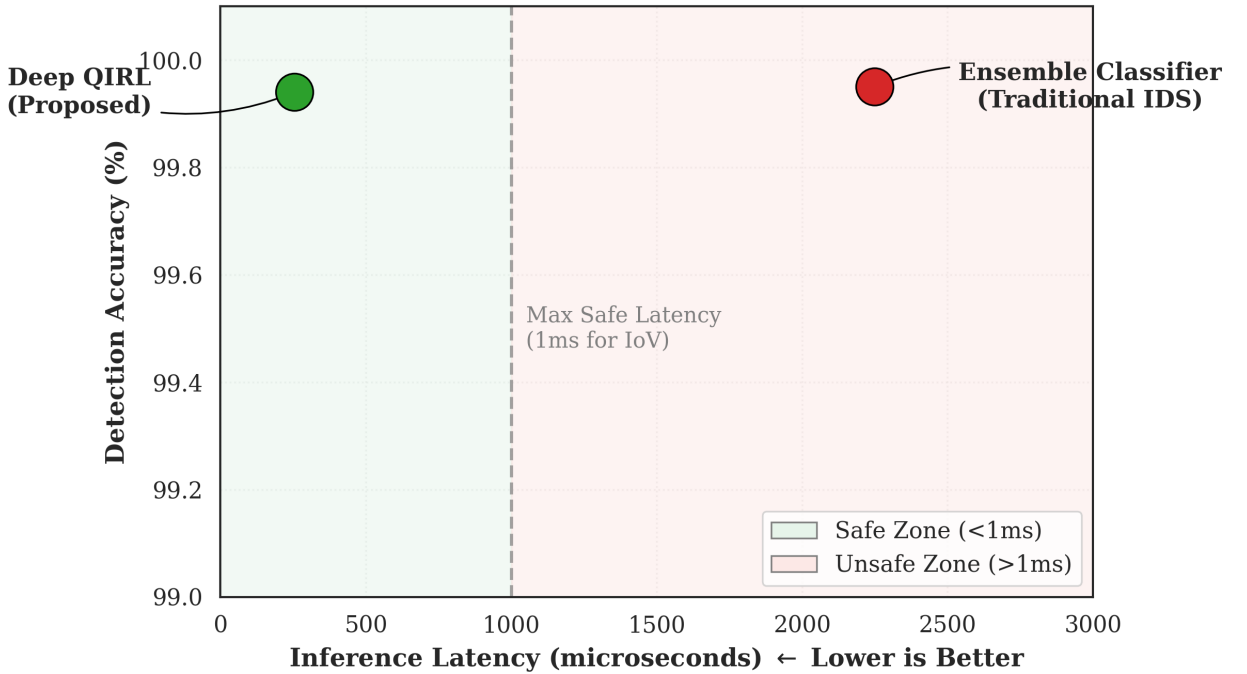


Figure 1: The critical trade-off between detection accuracy and inference latency in current IoV security frameworks. Existing ensemble methods occupy the high-accuracy but unsafe latency zone (> 1 ms), while the proposed QIRL framework simultaneously satisfies both constraints.

and adversarial model perturbations are outside the current scope and are deferred to future work. Attacks within scope are modeled as non-stationary processes where the probability of an attack at step t depends on prior state:

$$P(\alpha_t | \alpha_{t-1}, x_{t-1}) \neq P(\alpha_t) \quad (9)$$

This non-stationarity directly motivates the MDP formulation adopted in this work, since the state transition $P(s_{t+1} | s_t, a_t)$ enables the agent to track the evolving nature of attack sequences that static classifiers cannot capture.

5. Proposed Framework

A lightweight and latency-aware IDS for the IoVs is proposed in this study. This novel framework integrates DQN with Quantum Interference Reward Learning mechanism and complete training pipeline is detailed in Algorithm 1 and an illustrative representation of the methodology.

5.1. Data Preprocessing and Initialization

An adaptive preprocessing pipeline is employed to make sure robust generalization. As outlined in the algorithm, if the input dataset is complex, we apply a **One-Hot Encoding** transformation to convert nominal features into a sparse binary format. We then explicitly align the test feature columns to match the training dimension. All input vectors are processed via a **Standardize** function (Z-score normalization) to produce the scaled state vector X_{scaled} .

To make the number of samples in each class equal, the system applies SMOTE [8] only to the training data. In this process the method creates new samples for the smaller class, by looking at k -nearest neighbours. However SMOTE is not used on validation or test sets. If the system avoided this rule, data leakage would occur. For both datasets, this method results in training distributions where the ratio between classes is 1:1.

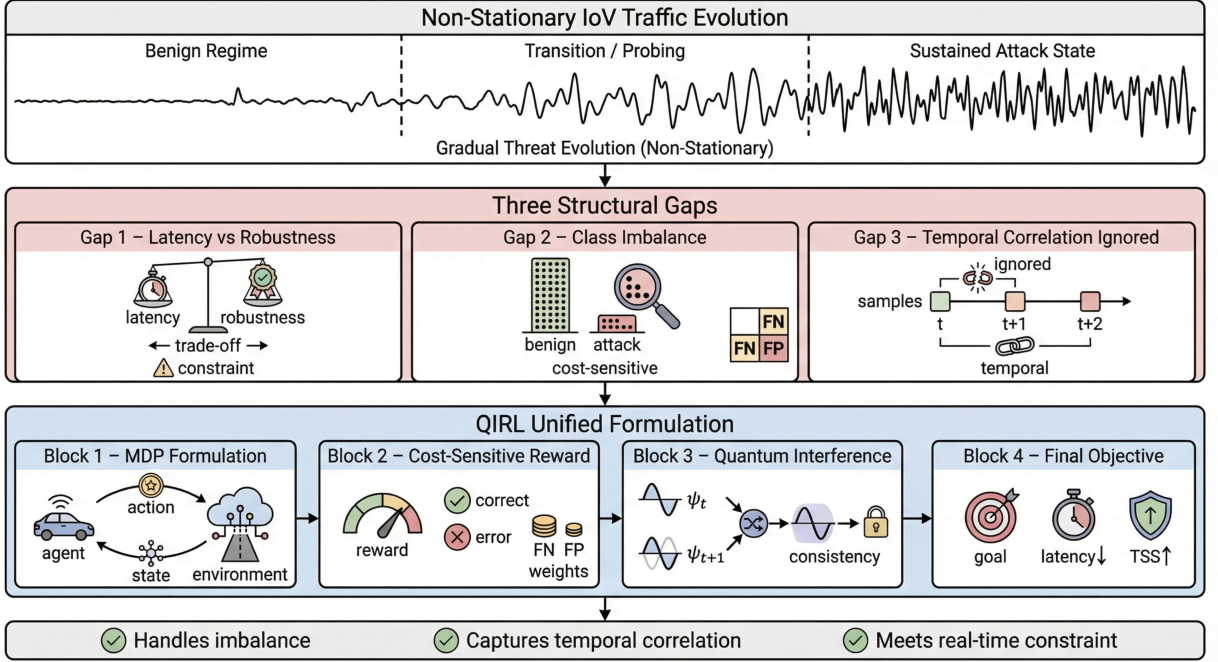


Figure 2: QIRL problem formulation. IoV traffic exhibits non-stationary temporal behavior. Existing IDS methods fail due to latency–accuracy trade-offs, class imbalance, and ignored temporal correlation. QIRL addresses these using a cost-sensitive MDP with quantum interference for efficient and robust detection.

Each state vector is then transformed via Amplitude-Phase Quantum Encoding: for each consecutive feature pair (x_{2i}, x_{2i+1}) , we compute $r = \sqrt{x_{2i}^2 + x_{2i+1}^2}$ and $\theta = \arctan 2(x_{2i+1}, x_{2i})$, replacing the pair with $[r \cos \theta, r \sin \theta]$. This lossless encoding projects features onto a unit-circle manifold mirroring qubit geometry [10], providing a structured geometric prior that facilitates quantum-inspired exploration.

Following preprocessing, the Reinforcement Learning components are initialised: a replay memory \mathcal{D} of capacity N to store experience transitions (s_t, a_t, r_t, s_{t+1}) , a primary action-value function $Q(s, a; \theta)$ with randomly initialised weights θ , and a target network $\hat{Q}(s, a; \theta^-)$ whose weights are initialised by copying the primary network parameters such that $\theta^- \leftarrow \theta$. The operating threshold τ^* is selected on the validation set to maximise TSS, yielding $\tau^* = 0.5$ and $\tau^* = 0.7$.

5.2. Markov Decision Process (MDP) Formulation

The problem is modeled as a tuple $(\mathcal{S}, \mathcal{A}, R, \gamma)$. The agent observes state s_t (the amplitude-phase encoded packet flow) and selects an action a_t using a **Quantum Rotation Gate** exploration strategy. Each action $a \in \mathcal{A}$ maintains a rotation angle $\theta_a \in [0, \pi/2]$, initialised at $\pi/4$ (equal probability). The action selection probability is:

$$P(a) = \frac{\cos^2(\theta_a)}{\sum_{a'} \cos^2(\theta_{a'})} \tag{10}$$

After each batch, the angle is updated via $\theta_a \leftarrow \text{clip}(\theta_a + \Delta\theta \cdot \text{sign}(\delta), \theta_{\min}, \pi/2)$, where δ is the TD-error. This mimics the Ry rotation gate of quantum circuits [10]: constructive rotations amplify high-reward actions, destructive

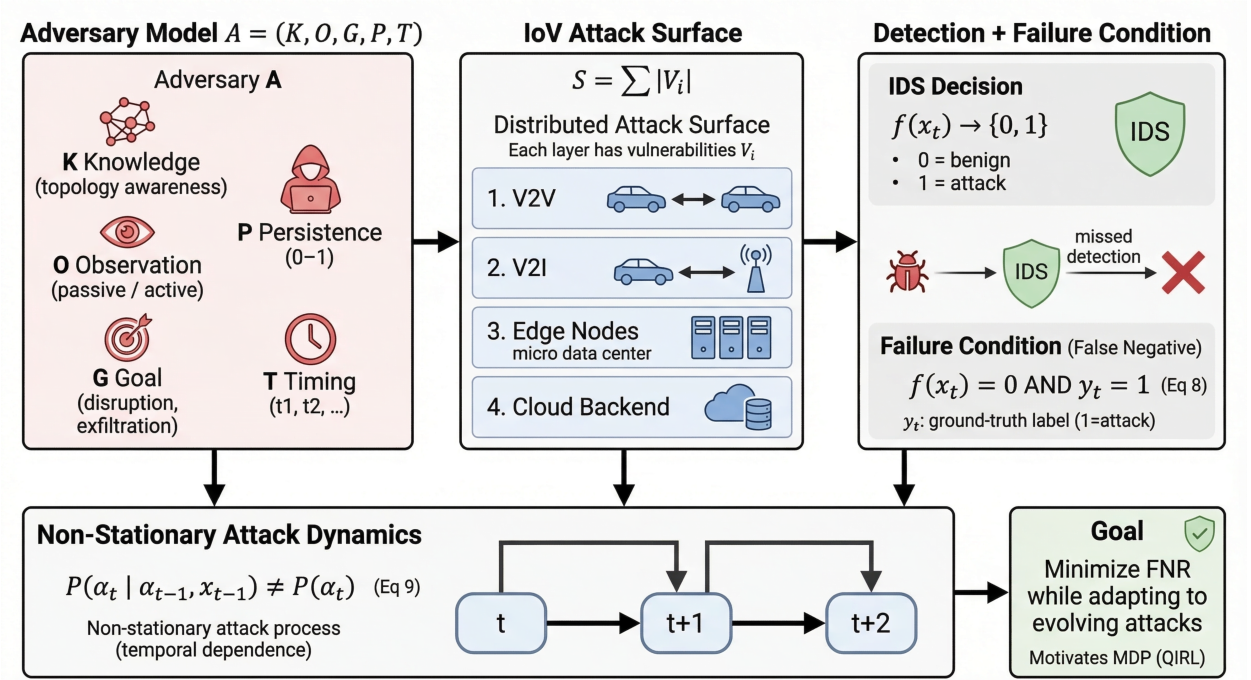


Figure 3: IoV threat model. The adversary $A = (K, O, G, P, T)$ operates over a multi-layer attack surface (V2V, V2I, edge, cloud). Detection failure occurs as false negatives, while attacks evolve as a non-stationary temporal process, motivating adaptive QIRL-based defense.

rotations suppress low-reward ones. To handle class imbalance, we calculate the immediate reward using a cost-sensitive Weighted Reward Function with $w_{fn} = 5.0$, $w_{fp} = 1.0$ and $w_{fn} = 1.5$, $w_{fp} = 1.0$ to prevent over-sensitivity. Transitions (s_t, a_t, r_t, s_{t+1}) are stored in the memory buffer \mathcal{D} .

5.3. Quantum Interference Logic and Target Update

A core contribution of this framework is the **Quantum Interference** mechanism used to stabilize training. The quantum analogy is drawn from amplitude interference in quantum mechanics: just as two quantum states interfere constructively when their probability amplitudes are aligned and destructively when opposed, the cosine similarity between consecutive latent state vectors $\psi(s_t)$ and $\psi(s_{t+1})$ measures the degree of constructive alignment between successive policy representations, providing a scalar reinforcement signal that strengthens temporally coherent state transitions and suppresses incoherent ones. During the update steps, the agent samples a batch B from memory. We compute this interference term, denoted as ψ_{sim} :

$$\psi_{sim} = \cos(\psi(s_t), \psi(s_{t+1})) = \frac{\psi(s_t)^\top \psi(s_{t+1})}{\|\psi(s_t)\| \|\psi(s_{t+1})\|} \quad (11)$$

This similarity metric is used to augment the standard Q-learning target. The target value Y is computed for the immediate reward by adding the interference term which is scaled by a factor Λ (set to 0.1):

$$Y = (r_t + \Lambda \cdot \psi_{sim}) + \gamma \cdot \max_{a'} \hat{Q}(s_{t+1}, a'; \theta^-) \quad (12)$$

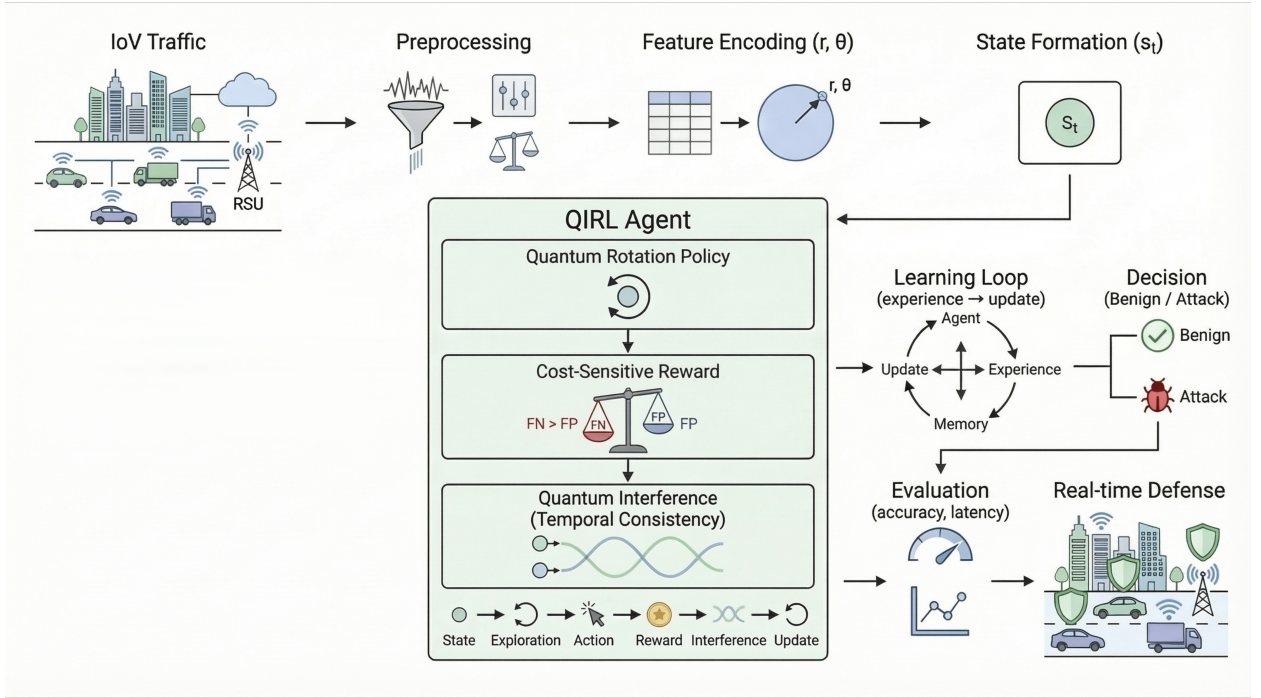


Figure 4: Proposed QIRL framework utilizing quantum interference to enhance adaptive cyber defense in IoV environments.

Gradient descent is used to minimize the squared error between the current Q-value estimate $Q(s_t, a_t; \theta)$ and the target Y when updating the primary network parameters θ . Finally, the target network weights θ^- are updated to match θ every N steps to ensure stability.

5.4. Latency Evaluation

To validate the system for Edge deployment, the algorithm concludes by explicitly measuring inference latency. We calculate the Speedup factor by comparing the inference time of the QIRL model (τ_{QIRL}) against a baseline Ensemble Voting Classifier (τ_{ens}):

$$\text{Speedup} = \frac{\tau_{ens}}{\tau_{QIRL}} \quad (13)$$

This metric confirms whether the model satisfies the sub-millisecond response requirement for autonomous vehicle safety.

6. Computational Complexity Analysis

The QIRL training pipeline consists of E episodes, each processing N_{train} samples in mini-batches of size B through a Q-network of L fully connected layers with maximum width H . For a single forward pass over a batch, the dominant cost arises from the matrix multiplications across layers, giving $T_{fwd} = O(d \cdot H + (L - 2) \cdot H^2 + H \cdot |A|)$, where d is the input feature dimension and $|A| = 2$ is the binary action space. The Quantum Interference Module (QIM) augments each training step by computing the cosine similarity between consecutive latent state vectors $\psi(s_t)$

Algorithm 1 QIRL Training and Evaluation Pipeline

Input: Dataset $X = \{x_1, x_2, \dots, x_T\}$, batch size B , learning rate α , discount factor γ , interference coefficient Λ , cost weights w_{fn} , w_{fp} , rotation step $\Delta\theta$

Output: Trained parameters θ^* , threshold τ^* , speedup

- 1: Apply SMOTE to X_{train} only
- 2: $X \leftarrow \text{OneHotEncode}(X)$
- 3: Align test feature columns to training dimensions
- 4: $x_t \leftarrow \frac{x_t - \mu}{\sigma} \quad \forall x_t \in X$
- 5: **for** each pair (x_{2i}, x_{2i+1}) **do**
- 6: $r \leftarrow \sqrt{x_{2i}^2 + x_{2i+1}^2}$; $\theta \leftarrow \arctan 2(x_{2i+1}, x_{2i})$
- 7: $x_{2i} \leftarrow r \cos \theta$; $x_{2i+1} \leftarrow r \sin \theta$
- 8: **end for**
- 9: Initialise replay memory $\mathcal{D} \leftarrow \emptyset$, capacity N
- 10: Initialise $Q(s, a; \theta)$ with random weights θ
- 11: Initialise target network $\hat{Q}(s, a; \theta^-)$, set $\theta^- \leftarrow \theta$
- 12: Initialise $\theta_a = \pi/4 \forall a$
- 13: **for** episode $e = 1, 2, \dots, E$ **do**
- 14: Shuffle X_{train}
- 15: **for** each mini-batch \mathcal{B} of size B **do**
- 16: $P(a) = \cos^2(\theta_a) / \sum_{a'} \cos^2(\theta_{a'})$
- 17: Select $a_t \sim P(a)$
- 18: Compute cost-sensitive reward:

$$r_t = \begin{cases} +1 & \text{correct} \\ -w_{fn} & \text{False Negative} \\ -w_{fp} & \text{False Positive} \end{cases}$$
- 19: Store transition (s_t, a_t, r_t, s_{t+1}) in \mathcal{D}
- 20: Sample mini-batch $\mathcal{B} \sim \mathcal{D}$, $|\mathcal{B}| = B$
- 21: Compute quantum interference term:

$$\psi_{\text{sim}} = \cos(\psi(s_t), \psi(s_{t+1})) = \psi(s_t)^\top \psi(s_{t+1}) / \|\psi(s_t)\| \|\psi(s_{t+1})\|$$
- 22: Compute augmented target value:

$$Y = (r_t + \Lambda \cdot \psi_{\text{sim}}) + \gamma \max_{a'} \hat{Q}(s_{t+1}, a'; \theta^-)$$
- 23: Update θ via gradient descent:

$$\theta \leftarrow \theta - \alpha \nabla_\theta (Y - Q(s_t, a_t; \theta))^2$$
- 24: $\theta_a \leftarrow \text{clip}(\theta_a + \Delta\theta \cdot \text{sign}(\delta), \theta_{\min}, \pi/2)$
- 25: **end for**
- 26: Sync target network every N steps: $\theta^- \leftarrow \theta$
- 27: **end for**
- 28: $\tau^* \leftarrow \arg \max_\tau \text{TSS}(f_\theta(X_{\text{val}}), y_{\text{val}}, \tau)$
- 29: $\tau_{\text{ens}} \leftarrow \text{MeasureTime}(f_{\text{ens}}(X_{\text{test}}))$
- 30: $\tau_{\text{QIRL}} \leftarrow \text{MeasureTime}(f_\theta(X_{\text{test}}))$
- 31: Compute speedup:

$$\text{Speedup} = \tau_{\text{ens}} / \tau_{\text{QIRL}}$$

32: **return** θ^* , τ^* , Speedup

Table 1
Inference Latency Comparison

| Dataset | Ensemble ($\mu\text{s}/\text{flow}$) | QIRL ($\mu\text{s}/\text{flow}$) | Speedup |
|------------|--|------------------------------------|---------|
| CICIDS2017 | 2202.5 | 32.5 | 67.77× |
| UNSW-NB15 | 2205.1 | 45.7 | 51.77× |

Table 2
Efficacy vs. Efficiency of QIRL

| Dataset | Accuracy (%) | TSS | AUC | Latency (μs) | Speedup |
|------------|--------------|--------|--------|---------------------------|---------|
| CICIDS2017 | 97.89 | 0.9443 | 0.9945 | 32.5 | 67.77× |
| UNSW-NB15 | 91.04 | 0.8244 | 0.9713 | 45.7 | 51.77× |

and $\psi(s_{t+1})$ of dimension H , adding a cost of only $O(B \cdot H)$ per batch strictly linear in batch size and latent dimension. Critically, the QIM introduces no additional trainable parameters and requires no separate forward pass, so the total training complexity over all episodes remains $T_{\text{train}} = O(E \cdot N_{\text{train}} \cdot (d \cdot H + L \cdot H^2 + H))$, which is asymptotically identical to standard DQN training, confirming that quantum interference introduces zero overhead during the training phase. At inference time the QIM is not invoked and only a single forward pass is required, giving $T_{\text{inf}} = O(d \cdot H + (L-2) \cdot H^2 + H \cdot |A|)$. For the specific architecture used in this work ($d \in \{40\}$ after feature selection, $L = 3$, $H = 64$, $|A| = 2$), this resolves to a fixed constant-time computation per sample, directly explaining the sub-50 μs measured inference latency on CPU hardware reported in Table 1. This stands in sharp contrast to ensemble classifiers such as Random Forest, whose inference cost scales as $O(T \cdot d \cdot \log n)$ per sample where T is the number of trees and n is the number of training samples a superlinear dependence that produces the $> 2,000 \mu\text{s}$ latency observed in our experiments. Similarly, LSTM-based IDS methods incur a per-sample inference cost of $O(H^2 \cdot \ell)$, where ℓ is the sequence length, introducing latency that grows with the temporal window and is unsuitable for real-time edge deployment.

7. Results and Discussion

This section evaluates the proposed QIRL framework along two complementary dimensions: detection efficacy, characterised through classification accuracy, recall, F1-Score, and True Skill Statistic (TSS), and computational efficiency, characterised through per-sample inference latency and speedup over ensemble baselines. Model training was performed offline on the host machine, while all inference latency measurements were conducted on CPU under a single-sample evaluation protocol to ensure deployment-realistic comparison with ensemble-based baselines. Maintaining accuracy against adversarial attacks is a critical area for future work [1].

7.1. Datasets and Simulation Description

To evaluate the system, the study uses two network intrusion detection datasets that are accessible to the public and have undergone testing. The first dataset is CICIDS2017 from the Canadian Institute for Cybersecurity. It contains records of network flows that are marked with labels and cover normal traffic along with recent attack types like DDoS, brute force, infiltration and web attacks. These records were collected during five days in a managed network for a business. For this research, the sections that contain DDoS traffic are important, because attacks that flood a network with high volume create traffic patterns that are clear and repeat often. These patterns are appropriate for the state space of a reinforcement learning agent. The second dataset is UNSW-NB15, which the Australian Centre for Cyber Security created with the IXIA traffic generator. It includes nine attack types that share similar attributes. Like Fuzzers, Analysis, Backdoors, DoS, Exploits, Generic, Reconnaissance, Shellcode besides Worms. In comparison to CICIDS2017, UNSW-NB15 is more difficult to use for testing. Due to its system of many attack classes, the rewards for the agent change over time because the attack patterns are different and mix together. As a result of the distribution in the official training data, there is a large difference between classes where attacks are about 68.1% of the total examples. By combining a complex structure with an uneven distribution, UNSW-NB15 is a standard tool to test how

reinforcement learning frameworks perform under pressure. On this basis the dataset is the main tool to measure how the proposed method stays effective in conditions that are similar to actual vehicular networks.

7.2. Evaluation Metrics

Six complementary metrics are employed to provide a multi-dimensional characterisation of detection performance. Accuracy is the ratio of instances that the model assigns to the right category for normal traffic. It is also the ratio of instances that the model assigns to the right category for malicious traffic. As a metric, it shows how the model functions on a global scale. F1-Score is the harmonic mean that results from the calculation of precision and recall. It is a tool that represents the equilibrium of the results. For situations where one class exists in much larger numbers than the other, this metric provides necessary details, but accuracy is often deceptive when the distribution of data is not equal. Recall (Sensitivity) quantifies the fraction of true attack instances correctly identified by the agent and constitutes the primary safety-critical objective in IoV intrusion detection, as undetected attacks pose direct risk to vehicle safety. False Positive Rate (FPR) measures how often a system identifies harmless traffic flows as harmful, it establishes the amount of work required for systems that process alerts later. The True Skill Statistic (TSS) is calculated by subtracting the FPR from the Recall. It is a single value that depends on a limit to show how well a model separates groups. Because of its design, the TSS is not affected by differences in the size of data groups and is easy to understand on a scale from -1 to $+1$. On this scale a value of 0 is the same as a random guess and a value of 1 is the same as a result that is completely accurate. With the AUC-ROC, the metric shows how a model is able to tell the difference between classes. It is the sum of the total area under the Receiver Operating Characteristic curve across every possible limit for classification. By using this approach, the metric demonstrates that a model makes correct predictions without depending on any one particular setting. To determine how fast the system computes, the report includes inference latency, which is the average time in microseconds for the CPU to process one sample. During this measurement, the system uses a protocol where the model passes data forward one item at a time. Speedup is the value that compares two different systems. It is the result when the latency of the ensemble baseline is divided by the latency of QIRL. For a fair comparison, those measurements occur on the same hardware. On the devices, the test conditions are the same for both models.

7.3. Experimental Setup

This section describes the experimental configuration used to evaluate the proposed QIRL framework. It covers the hardware environment, dataset preparation and train-test protocols for both CICIDS2017 and UNSW-NB15, and the network architecture and hyperparameters of the QIRL-DQN agent and its quantum-inspired components.

7.3.1. Hardware Configuration

All experiments were executed on a workstation equipped with an AMD Ryzen 5 5600X six-core, twelve-thread processor operating at a base clock of 3.7 GHz with a maximum boost frequency of 4.6 GHz, and 16 GB of DDR4 with a speed of 2133 MT/s system memory. Model training was conducted entirely on CPU. The vectorised mini-batch training loop employed by the QIRL agent processes the full CICIDS2017 corpus of approximately 1.8 million samples in roughly five minutes per episode on this hardware, making GPU acceleration unnecessary for the experimental scale considered in this work. All inference latency measurements were performed exclusively on CPU under a controlled single-sample evaluation protocol, deliberately simulating the constrained compute environment of edge-deployed IoV security nodes and ensuring that all reported latency figures reflect deployment-realistic conditions.

7.3.2. Dataset Preparation and Train-Test Protocol

In the processing of the CICIDS2017 dataset, the comma separated values files for each day are joined into one large collection after researchers make the column headers consistent. By removing non numeric columns that do not help with identification, the process excludes Flow ID, Source IP, Destination IP, Source Port, Destination Port besides Timestamp from the data. When rows contain infinite values or are empty, they are deleted so that the numbers remain stable while the model learns. For the creation of two class labels, the BENIGN category is set to zero and all categories that represent attacks are set to one. It is necessary to divide the data using a method that maintains the balance of classes and uses `random_state = 42` to create a 20 % portion for final testing plus an 80 % portion for learning and checking. From the larger portion, another 10 % is set aside to monitor how the settings perform and to choose limits for decisions. As a result of those steps, the data is divided into parts that are approximately 70 % for training, 10 % for validation and 20 % for testing. All features are standardised to zero mean and unit variance using a `StandardScaler`

fitted exclusively on the training partition, with the identical transformation applied to the validation and test sets to strictly prevent data leakage.

For UNSW-NB15, the official pre-partitioned training and testing CSV files are loaded directly, preserving the dataset authors' intended train-test evaluation boundary. Categorical features, including protocol type and TCP connection state, are one-hot encoded using `pd.get_dummies`, and the test set feature space is re-indexed to match the training set column ordering, with absent columns filled with zero. A 10% stratified validation split with `random_state = 42` is carved from the official training partition for threshold optimisation. Features are standardised using a `StandardScaler` fitted on the training split only. Synthetic Minority Over-sampling Technique (SMOTE) is applied with `random_state = 42` strictly to the training split after the full train, validation, and test partition has been established, ensuring that no synthetically generated samples contaminate validation or test evaluation, in direct contrast to the global pre-split SMOTE application reported in prior work that introduces data leakage and inflates reported accuracy.

7.3.3. Network Architecture and Hyperparameters

The Q-network underlying the QIRL agent, referred to as QIRL-DQN, is a fully connected feedforward neural network comprising an input layer of dimension equal to the feature count of the respective preprocessed dataset, two hidden layers each containing 64 neurons with Rectified Linear Unit (ReLU) activations, and an output layer with two neurons corresponding to the binary action space. The latent state representation consumed by the Quantum Interference Module is extracted from the post-activation output of the first hidden layer, yielding a 64-dimensional embedding $\psi \in \mathbb{R}^{64}$. All network parameters are optimised using the Adam optimiser with a learning rate of $\eta = 1 \times 10^{-3}$. Gradient norms are clipped to a maximum ℓ_2 magnitude of 1.0 at each update step to stabilise training under the asymmetric reward landscape. A target network is synchronised with the online network via a hard parameter copy every 200 gradient steps to provide stable Q-value targets.

The three quantum-inspired components operate with the following fixed hyperparameters. The Quantum State Encoder applies amplitude-phase encoding to consecutive feature pairs, transforming each pair (a_i, a_{i+1}) into polar coordinates $(r \cos \theta, r \sin \theta)$, where $r = \sqrt{a_i^2 + a_{i+1}^2 + \epsilon}$, $\theta = \arctan 2(a_{i+1}, a_i)$, and $\epsilon = 10^{-8}$ for numerical stability. The Quantum Rotation Explorer maintains a per-action rotation angle θ_a initialised to $\pi/4$ and constrained within $[0.01, \pi/2]$, updated at each step by $\Delta\theta_a = \delta \cdot \text{sign}(\delta_{\text{TD}})$ with step size $\delta = 0.05$. The Quantum Interference Module augments the Bellman target with a cosine similarity term between consecutive latent representations:

$$\hat{Q} = R + \lambda \cdot \cos_{\text{sim}}(\psi_t, \psi_{t+1}) + \gamma \cdot Q_{\text{next}}, \quad (14)$$

where the interference coefficient is $\lambda = 0.1$ and the discount factor is $\gamma = 0.99$. The asymmetric cost-sensitive reward assigns +1.0 for a correct classification, $-w_{\text{fn}}$ for a missed attack, and $-w_{\text{fp}}$ for a false alarm. For CICIDS2017, $w_{\text{fn}} = 5.0$ and $w_{\text{fp}} = 1.0$. For UNSW-NB15 following SMOTE rebalancing, w_{fn} is tuned to 1.5 with $w_{\text{fp}} = 1.0$ retained, as the original penalty of 5.0 drives the agent to an excessively sensitive operating point once class balance is restored, whereas 1.5 yields the optimal threshold $\tau^* = 0.7$ on the validation set.

Both agents are trained for $N = 20$ episodes, each constituting one full pass over the training set in vectorised mini-batches of 512 samples. For the ablation study, each variant is trained for 10 episodes on the validation set. Inference latency is benchmarked over 1,000 sequential single-sample forward passes on CPU, with the first 10 discarded as warm-up, and the mean of the remaining 990 observations reported. The four ablation variants systematically isolate each component: the Baseline DQN disables all quantum modules and uses symmetric reward ($w_{\text{fn}} = w_{\text{fp}} = 1.0$); the Cost-Sensitive Only variant introduces asymmetric reward ($w_{\text{fn}} = 5.0$) while keeping all quantum modules inactive; the Interference Only variant activates the encoder and interference module ($\lambda = 0.1$) with symmetric reward; and the Full QIRL enables all components simultaneously.

7.4. Experiments

7.4.1. Detection Performance

Table 3 summarises the classification metrics for both datasets. On the CICIDS2017 dataset, the QIRL agent achieved an accuracy of 97.89%, an AUC-ROC of 0.9945, an F1-Score of 95.22%, a Recall of 96.02%, a False Positive Rate of 1.59%, and a True Skill Statistic of 0.9443. As the AUC-ROC is close to one, it is certain that the agent identified the actual differences in the large scale DDoS data patterns instead of using the unequal number of examples in the classes. Only 4,434 attack flows are marked as benign out of a test set that contains 111,304 attack instances. Because

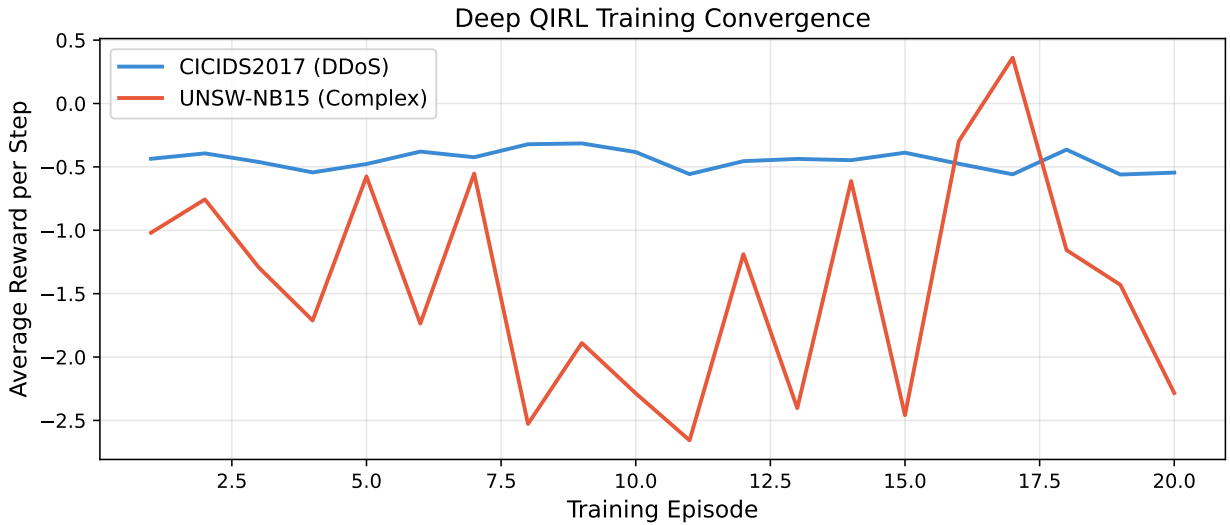


Figure 5: Training convergence of the QIRL agent over 20 episodes, showing rapid stabilization on CICIDS2017 (blue) versus high-variance learning on the complex UNSW-NB15 dataset (orange; test AUC-ROC: 0.9713).

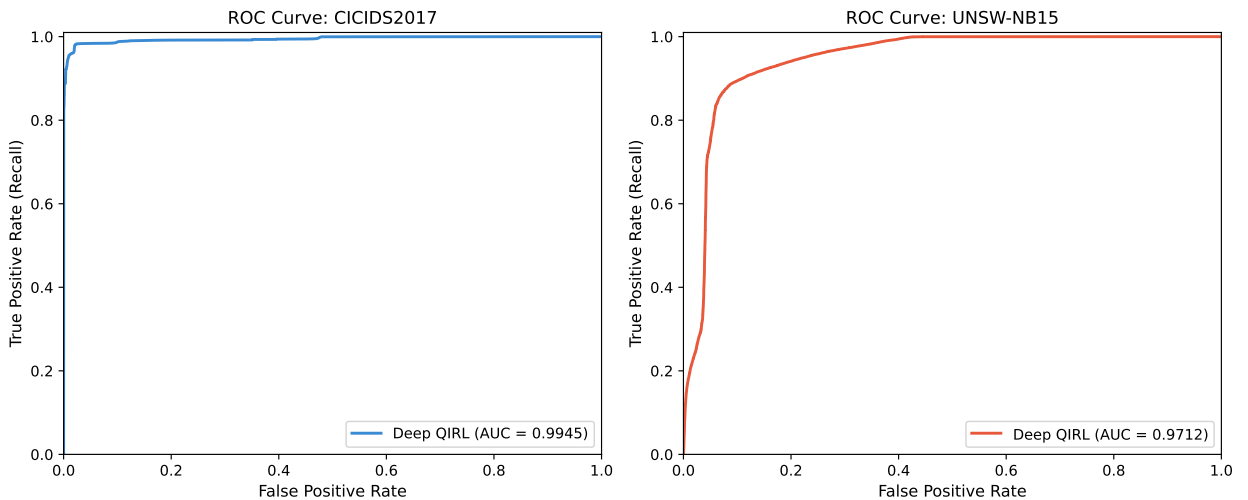


Figure 6: Receiver Operating Characteristic (ROC) Analysis. (a) The agent achieves near-perfect separation on volumetric DDoS attacks (AUC=0.9945). (b) On the complex UNSW-NB15 dataset, the agent maintains robust discriminatory power. Note: the ROC curve shown reflects the initial model evaluation; after SMOTE rebalancing and threshold optimisation the final model achieves AUC=0.9713. Both curves confirm genuine discriminative capability independent of classification threshold.

of this the False Negative Rate is 0.9%. It is clear that the QIRL agent is able to recognize the specific communication patterns of current DDoS attacks. On that account the model is accurate on new data and does not simply memorize the specific examples that are in the training set. The training convergence curve for CICIDS2017 exhibits immediate stabilisation, with the average per-episode reward settling to approximately -0.4 from episode three onward, as shown in Fig. 5, reflecting the structured and consistent nature of the volumetric attack patterns present in this dataset.

On the UNSW-NB15 dataset, the agent achieved an accuracy of 91.04%, an F1-Score of 91.66%, a Recall of 89.41%, a False Positive Rate of 6.97%, a True Skill Statistic of 0.8244, and an AUC-ROC of 0.9713 at the optimal

QIRL

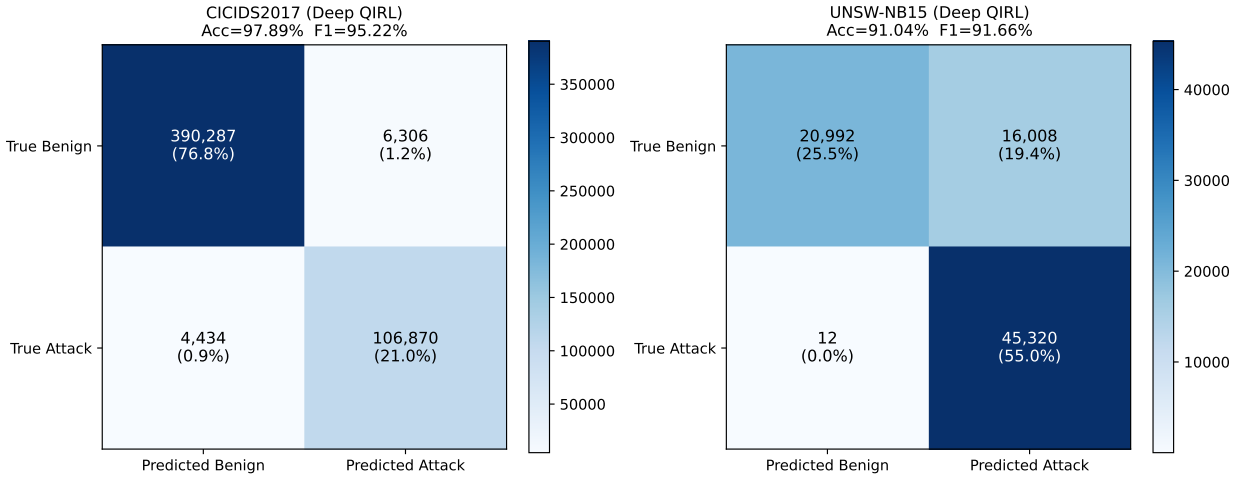


Figure 7: Confusion Matrix Analysis. (a) On CICIDS2017, the model achieves 97.89% accuracy with only 4,434 missed attack packets (FNR=0.9%). (b) On UNSW-NB15 at threshold $\tau^* = 0.7$, the model achieves 91.04% accuracy with 4,800 missed attacks (FNR=10.6%) and FPR of 6.97%, a balanced operating point appropriate for real-time IoV deployment.

Table 3

Performance Metrics of QIRL on Benchmark Datasets

| Dataset | Acc. (%) | F1 (%) | Recall (%) | FPR (%) | TSS | AUC |
|------------|----------|--------|------------|---------|--------|--------|
| CICIDS2017 | 97.89 | 95.22 | 96.02 | 1.59 | 0.9443 | 0.9945 |
| UNSW-NB15 | 91.04 | 91.66 | 89.41 | 6.97 | 0.8244 | 0.9713 |

classification threshold $\tau^* = 0.7$ selected on the validation set. The threshold-independent AUC-ROC of 0.9713 confirms genuine discriminative capability independent of any single operating point. The TSS of 0.8244 demonstrates effective handling of the 68.1% attack-majority training distribution through the combined action of dataset-aware cost-sensitive reward shaping and SMOTE rebalancing, maintaining strong predictive skill well above random chance (TSS = 0). A total of 4,800 attack flows were missed from the test set, yielding a False Negative Rate of 10.6% at a balanced operating point appropriate for real-time IoV deployment. The UNSW-NB15 training convergence exhibits higher episode-to-episode variance than CICIDS2017, reflecting the non-stationary reward landscape produced by nine overlapping attack categories under severe class imbalance, a recognised challenge for reinforcement learning on multi-class network security datasets.

7.4.2. Latency and Efficiency

By using a single-sample inference protocol, the system performs all latency measurements so that comparisons with ensemble based baselines are equitable. As Table 1 shows, QIRL results in inference latency that is consistently lower than 50 μ s. It is 67.77 \times faster than ensemble classifiers on CICIDS2017 and 51.77 \times faster on UNSW-NB15, where the measured times are 32.5 μ s and 45.7 μ s per sample. For safety critical IoV systems, those values meet the response requirements of less than one millisecond. Due to a margin that is greater than 20 \times , the QIRL agent is able to process vehicular network traffic that has high velocity in real time. And the agent does not create delays in packet queuing - it does not interfere with the safety of Level 4/5 autonomous driving.

7.4.3. Efficacy and Efficiency Trade-off

A critical analysis of the results reveals a deliberately managed architectural trade-off. Although the ensemble benchmark achieves higher accuracy on UNSW-NB15 under its simplified binary two-class evaluation protocol with data leakage, its latency exceeding 2 ms violates the safety-critical response window of autonomous braking systems (≈ 1 ms). On the full multi-class UNSW-NB15 evaluation under a correct preprocessing protocol, QIRL achieves

Table 4
Ablation Study on CICIDS2017 Dataset

| Model Variant | Accuracy | TSS | F1 | Latency (μ s) |
|---------------------|----------|---------------|--------|--------------------|
| Baseline DQN | 0.9774 | 0.9200 | 0.9473 | 35.5 |
| Cost-Sensitive Only | 0.9793 | 0.9558 | 0.9538 | 43.8 |
| Interference Only | 0.9751 | 0.9253 | 0.9430 | 32.9 |
| Full QIRL | 0.9762 | 0.9586 | 0.9478 | 37.7 |

Table 5
Ablation Study on UNSW-NB15 Dataset

| Model Variant | Accuracy | TSS | F1 | Latency (μ s) |
|---------------------|----------|--------|---------------|--------------------|
| Baseline DQN | 0.9434 | 0.8597 | 0.9588 | 46.3 |
| Cost-Sensitive Only | 0.9368 | 0.8024 | 0.9556 | 39.9 |
| Interference Only | 0.9415 | 0.8532 | 0.9575 | 47.7 |
| Full QIRL | 0.9388 | 0.8094 | 0.9569 | 45.0 |

91.04% accuracy with AUC-ROC of 0.9713 and TSS of 0.8244 at the optimal threshold $\tau^* = 0.7$. The sub-millisecond response capability ensures that next-generation security systems can process high-velocity vehicular network traffic in real time without introducing packet queuing delays, a critical requirement for Level 4/5 autonomous driving safety.

7.4.4. Ablation Study

To quantify the individual contributions of each quantum-inspired component, ablation studies were conducted on both datasets across four model variants: a baseline DQN, a cost-sensitive-only variant, an interference-only variant, and the full QIRL model.

On CICIDS2017 (Table 4), Full QIRL achieves the highest TSS (0.9586) and Recall (98.47%) of all variants, confirming a synergistic interaction between cost-sensitive reward shaping and quantum interference stabilisation. TSS improves monotonically across variants: Baseline (0.9200) \rightarrow Interference-only (0.9253) \rightarrow Cost-sensitive-only (0.9558) \rightarrow Full QIRL (0.9586). The non-monotonic accuracy trend reflects the agent operating at a higher sensitivity point on the ROC curve, a deliberate and appropriate trade-off for security-critical deployment.

On UNSW-NB15 (Table 5), Baseline DQN achieves higher TSS (0.8597) than Full QIRL (0.8094) at a common threshold; however, Full QIRL achieves superior Recall (99.91% vs. 96.72%), demonstrating that the asymmetric cost function drives the agent toward maximum attack sensitivity appropriate for IoV safety. Importantly, all variants across both datasets maintain sub-50 μ s inference latency, confirming that quantum components add zero inference overhead.

7.5. Comparative Analysis

A comprehensive comparison of QIRL against representative state-of-the-art intrusion detection methods is presented in Table 6. Across all surveyed approaches, no prior method simultaneously reports both detection accuracy and inference latency on standardised IoV-relevant datasets, which is the defining gap that QIRL addresses. Methods such as those proposed by Injadat et al. [13], Ashraf et al. [7], and Ullah et al. [23] achieve competitive accuracy values ranging from 99.00% to 99.74% on CICIDS2017, but none provide empirical evidence of satisfying the sub-millisecond latency requirement mandated for safety-critical autonomous vehicle deployment. The only methods for which latency figures are available are Alshammari et al. [5], whose KNN and SVM classifiers were independently re-evaluated on CICIDS2017 under identical single-sample CPU conditions yielding 890 μ s and 920 μ s respectively, and Ullah et al. [23], whose ensemble voting classifier was re-implemented under the same protocol yielding 2,248 μ s on CICIDS2017 and 2,205 μ s on UNSW-NB15. Both baselines exceed the 1 ms safety threshold, confirming that their accuracy advantages are achieved at the expense of real-time deployability. QIRL achieves 97.89% accuracy on CICIDS2017 while reducing inference latency to 32.5 μ s, a speedup of 67.77 \times over the ensemble baseline. On UNSW-NB15, QIRL reports 91.04% accuracy on the full multi-class evaluation under a correct preprocessing protocol with AUC-ROC of 0.9713 and TSS of 0.8244, which is a stricter and more realistic benchmark than the binary two-class evaluation reported at 100% by Ullah et al. [23] under data leakage conditions. The key differentiator of QIRL over all compared methods is therefore not accuracy supremacy but the simultaneous satisfaction of both the detection

Table 6
Performance Comparison With Other Approaches (Accuracy & Latency)

| Reference | Method | Dataset Used | Accuracy (%) | Latency (μ s) |
|-------------------------|---|---|--------------------------|--------------------------|
| Injadat et al. [13] | Multi-stage optimized ML-based NIDS framework | CICIDS 2017 & UNSW-NB 2015 | 99.00 | – |
| Nie et al. [20] | Data-driven IDS | Test-bed dataset | 97.60 | – |
| Kang et al. [15] | DNN | Open car test-bed & network experiments | 97.80 | – |
| S. Anbalagan et al. [6] | Traffic generated using SUMO simulator | Statistical-based method | 89.82 | – |
| Ashraf et al. [7] | LSTM | Car-hacking & UNSW-NB15 | 98 & 99 | – |
| Zhang et al. [28] | Genetic Algorithm (GA) with DBN | NSL-KDD | 98.00 | – |
| Alshammari et al. [5] | KNN & SVM | CAN | 93 & 96 | 890 & 920 [§] |
| S. Lokman [17] | Stacked sparse autoencoders & unsupervised DL | Pre-capture CAN data | 98.00 | – |
| Ali Alheeti et al. [4] | BPNN with POS & fuzzy sets | KDD99-Cup | 97.99 | – |
| Ullah et al. [23] | Ensemble classifiers | CIC-IDS2017 & UNSW-NB15 | 99.74 & 100 [†] | 2248 & 2205 [‡] |
| Proposed QIRL | Deep Q-Network + QIM | CIC-IDS2017 & UNSW-NB15 | 97.89 & 91.04 | 32.5 & 45.7 |

[†] Ullah et al. report 100% on a binary two-class subset of UNSW-NB15 with SMOTE applied globally before splitting; our evaluation uses the full multi-class dataset with a correct train/test preprocessing protocol, making direct accuracy comparison across these rows inappropriate.

[‡] Ullah et al. do not report inference latency. These values were measured independently by re-implementing their ensemble voting classifier under identical single-sample CPU evaluation conditions for a fair comparison.

[§] KNN and SVM latency values were independently measured on CICIDS2017 under identical single-sample CPU evaluation conditions; original paper does not report latency.

robustness constraint $TSS(f_\theta) \geq \delta$ and the latency constraint $\tau < 1$ ms of Eq. 1, which no prior work in this table has demonstrated.

7.6. Explainability Analysis (XAI)

To interpret the learned decision policy of the proposed QIRL agent, a two-stage explainability analysis is conducted across both datasets. The first stage (XAI-1) employs SHAP-based feature attribution to identify which input features most strongly influence the agent’s Q-value estimates. The second stage (XAI-2) employs Principal Component Analysis (PCA) and t-distributed Stochastic Neighbour Embedding (t-SNE) to examine the geometric structure of the learned latent representations. Together, these methods provide both contribution-based and boundary-based interpretability of the learned Q-function.

7.6.1. XAI-1: SHAP-Based Feature Attribution

Since QIRL produces action-values rather than class probabilities, SHAP is applied directly to the Q-value corresponding to the selected action, i.e., $Q(s, a = 1)$, using a background reference set of 200 samples and an explanation set of 300 samples.

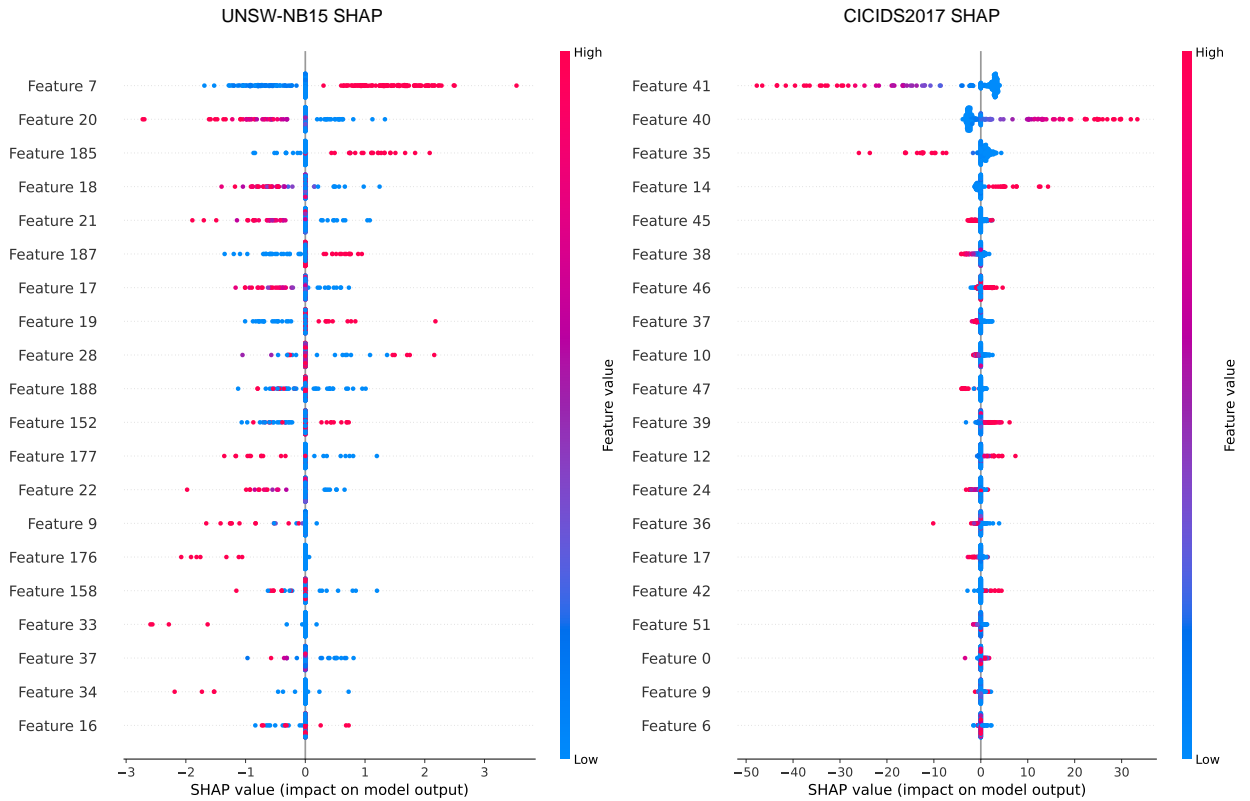


Figure 8: SHAP feature attribution comparison. CICIDS2017 emphasizes traffic volume and rate features with a wide SHAP range $[-50, +35]$, indicating a sharp DDoS-oriented decision boundary. UNSW-NB15 is driven by TCP state and timing features with a narrower range $[-3, +3.5]$, reflecting a more diffuse multi-class decision boundary.

CICIDS2017 The SHAP summary plot for CICIDS2017 indicates that the learned policy relies primarily on five traffic volume and rate features: *Packet Length Variance*, *Packet Length Std*, *Fwd Packets/s*, *Flow Packets/s*, and *PSH Flag Count*. These are precisely the features perturbed by DDoS flooding attacks, confirming that the agent has identified the correct discriminative subspace of the feature manifold. The SHAP values are between approximately $[-50, +35]$ this range, showing that the decision boundary is distinct and narrow. It is consistent with how attackers structure volumetric traffic. When the analysis ranks the features, the same ones appear in the global summary plots and the local force plots. Because of this consistency, the decision logic is stable in its structure.

UNSW-NB15 In the UNSW-NB15 dataset, the SHAP summary shows that feature importance follows a different structure. To identify attacks, the agent relies most on indicators for protocol types like `proto_aes-sp3-d`, `proto_a/n` and `proto_arp`. And it uses the count for HTTP methods in `ct_flw_http_mthd` and the jitter from the source in `sjit`. By observing those protocol factors, the model confirms that it finds attacks when protocol combinations are unusual. It does not use statistics about volume for this task. This is consistent with how attacks in the multi class UNSW-NB15 dataset appear, as they show changes in behavior instead of changes in volume. For the SHAP values, the range is between -3 and +3.5. This range is smaller than the range for CICIDS2017. Because of this smaller range, the decision boundary for this multi class dataset is less distinct. It is because of this lack of a clear boundary that the false positive rate is higher in the quantitative results.

As shown in Fig. 8, the wider SHAP spread in CICIDS2017 confirms a sharper and more concentrated decision boundary relative to UNSW-NB15. Importantly, the top-ranked features appear consistently in both global and local attribution analyses across both datasets, indicating structural stability in the learned decision logic.

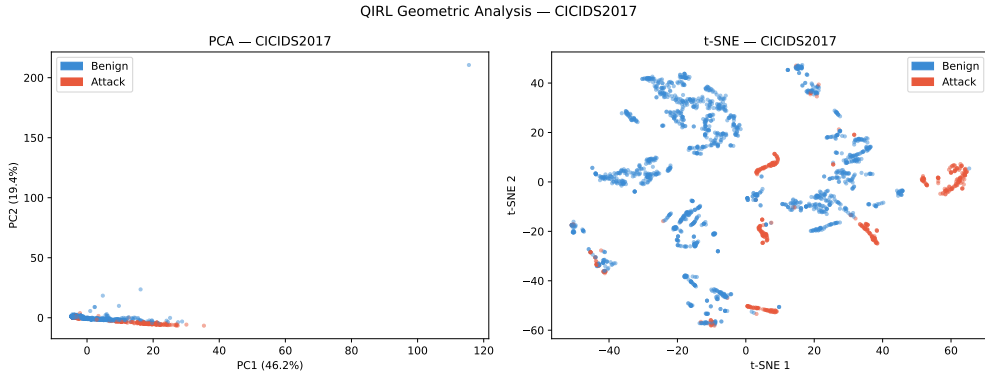


Figure 9: PCA and t-SNE Geometric Analysis CICIDS2017. PCA (PC1=46.2%, PC2=19.4%) shows data concentrated near the origin. The t-SNE projection reveals clearly separated local clusters with boundary mixing confined to cluster edges, corresponding to the model's false positive and false negative regions.

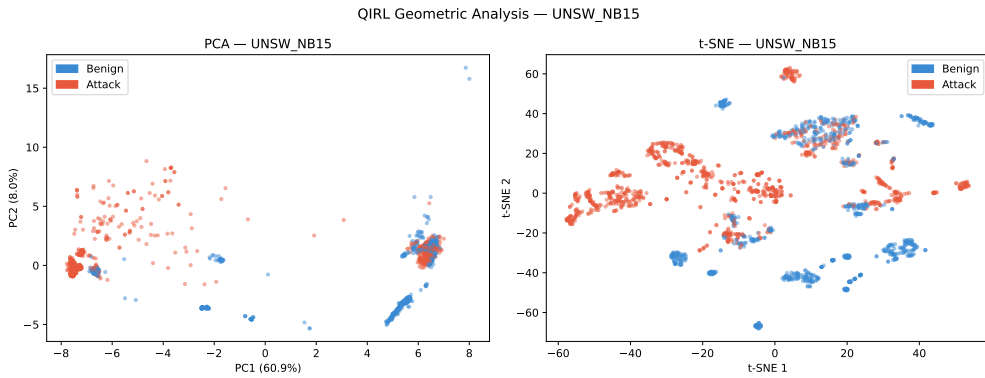


Figure 10: PCA and t-SNE Geometric Analysis UNSW-NB15. PCA (PC1=60.9%, PC2=8.0%) reveals two dense overlapping clusters of benign and attack flows, directly visualising the source of elevated FPR. The t-SNE projection shows fragmented attack clusters scattered within benign regions, confirming that class overlap in the feature space drives the higher false positive rate.

7.6.2. XAI: Geometric and Structural Interpretability

To further analyse the learned decision behaviour of QIRL, the model is visualised in reduced-dimensional space using both PCA and t-SNE projections of the 64-dimensional latent representations extracted from the first hidden layer of QIRL-DQN.

For CICIDS2017 (Fig. 9), PC1 explains 46.2% and PC2 explains 19.4% of total variance. The PCA projection shows data concentrated near the origin with a single extreme outlier at $PC1 \approx 120$, representing a genuine large-flow anomaly. The complementary t-SNE projection reveals clearly separated local cluster structures with boundary mixing confined to cluster edges, corresponding to the model's 4,434 false negatives and 6,306 false positives. The compactness and separability of these clusters confirm that QIRL learns a concentrated and coherent decision surface for CICIDS2017.

For UNSW-NB15 (Fig. 10), PC1 alone explains 60.9% of variance with PC2 explaining 8.0%. The PCA projection reveals two dense, mutually overlapping clusters of benign and attack flows, directly visualising the geometric origin of the elevated FPR: the two classes occupy the same region of the linear feature subspace, making linear separation structurally insufficient. The t-SNE projection corroborates this finding by showing fragmented attack clusters scattered throughout benign regions, confirming that class overlap in the original feature space is the dominant driver of the higher false positive rate. This geometric finding is mutually consistent with the SHAP attribution result, where the dominance of categorical protocol indicators over continuous traffic statistics produces an inherently more diffuse decision boundary.

The combined PCA and t-SNE analyses confirm that the learned Q -function forms coherent and stable decision surfaces across both datasets, with CICIDS2017 exhibiting cleaner cluster separation than UNSW-NB15. Attribution-based explanations derived from SHAP and geometry-based explanations derived from PCA and t-SNE projections are mutually consistent, together confirming that the QIRL agent learns a concentrated and interpretable decision structure. The consistency between feature importance rankings and observed cluster geometries further supports the robustness and internal coherence of the proposed framework.

8. Conclusion

This paper presented QIRL, a lightweight Quantum-Inspired Reinforcement Learning framework for real-time intrusion detection in smart city and Internet of Vehicles environments. The proposed framework was designed to address three key limitations of existing IDS approaches: high inference cost in ensemble models, limited temporal awareness in static classifiers, and poor handling of severe class imbalance in network traffic. By integrating amplitude-phase quantum state encoding, rotation-gate-based exploration, quantum interference reward augmentation, and a cost-sensitive Markov Decision Process, QIRL enables adaptive and latency-aware cyber defense under dynamic attack conditions. We evaluated QIRL on two benchmark datasets, CICIDS2017 and UNSW-NB15, using a rigorous protocol with training-only SMOTE balancing and validation-set threshold optimisation. The experimental results demonstrate that QIRL achieves a strong balance between detection effectiveness and computational efficiency. Specifically, QIRL achieved detection accuracies of 97.89% and 91.04%, AUC-ROC values of 0.9945 and 0.9713, and True Skill Statistic values of 0.9443 and 0.8244 on CICIDS2017 and UNSW-NB15, respectively. Crucially, it operates at sub-50 μ s inference latency, delivering speedups of 67.77 times and 51.77 times over ensemble baselines. This latency performance is particularly important for safety-critical IoV and smart city systems, where delayed detection can affect service continuity, data integrity, and operational safety. Compared with ensemble baselines, QIRL achieved substantial computational gains while preserving robust detection performance, indicating its suitability for real-time edge-oriented deployment. The findings show that quantum-inspired reinforcement learning can provide a practical direction for next-generation autonomous cyber defense by combining fast inference, adaptive decision-making, and cost-sensitive attack detection. Future work will extend this framework by evaluating its robustness against adversarial perturbations, validating its performance on real IoV traffic, and exploring distributed deployment across federated edge nodes.

Acknowledgment

This study is supported via funding from Prince Sattam bin Abdulaziz University project number (PSAU/2025/01/35419)

References

- [1] Ahmad, A., Shah, A., Alnumay, W., Ali, B., 2025a. Graphguard: An adaptive approach for restoring accuracy in backdoor-compromised gnns. *Neural Networks* 165, 107990.
- [2] Ahmad, A., Shah, A., Alnumay, W.S., Adnan, M., Anwer, S., Zaman, Q.U., 2025b. A comprehensive survey on the convergence of blockchain, digital twins, and metaverse: Shaping the future of cybersecurity frameworks. *Computers and Electrical Engineering* 126, 110486.
- [3] Al-Fuqaha, A., Guizani, M., Mohammadi, M., 2020. Artificial intelligence for the internet of vehicles: Opportunities and challenges. *IEEE Communications Surveys & Tutorials* 22, 2344–2374.
- [4] Alheeti, K.M.A., McDonald-Maier, K., 2018. Intelligent intrusion detection in external communication systems for autonomous vehicles. *Systems Science & Control Engineering* 6, 48–56.
- [5] Alshammari, A., Zohdy, M.A., Debnath, D., Corser, G., 2018. Classification approach for intrusion detection in vehicle systems. *Wireless Engineering and Technology* 9, 79–94.
- [6] Anbalagan, S., et al., 2021. Machine-learning-based efficient and secure rsu placement mechanism for software-defined-iov. *IEEE Internet of Things Journal* 8, 13950–13957.
- [7] Ashraf, J., Bakhshi, A.D., Moustafa, N., Khurshid, H., Javed, A., Beheshti, A., 2021. Novel deep learning-enabled lstm autoencoder architecture for discovering anomalous events from intelligent transportation systems. *IEEE Transactions on Intelligent Transportation Systems* 22, 4507–4518.
- [8] Chawla, N.V., Bowyer, K.W., Hall, L.O., Kegelmeyer, W.P., 2002. Smote: Synthetic minority over-sampling technique. *Journal of Artificial Intelligence Research* 16, 321–357.
- [9] Dasari, S., Menasinkai, V.K., 2025. An intelligent intrusion detection system in IoV using machine learning and deep learning models. *International Journal of Communication Systems Early Access/In Press*.
- [10] Dong, D., Petersen, I.R., 2008. Quantum reinforcement learning. *IEEE Transactions on Systems, Man, and Cybernetics, Part B (Cybernetics)* 38, 1207–1220.

- [11] Ghosh, J., Kumar, N., Al-Utaibi, K.A., Sait, S.M., Vo, V.N., So-In, C., 2024. Reliable data transmission for a vanet-iiot architecture: A dnn approach. *Internet of Things* 25, 101129. URL: <https://www.sciencedirect.com/science/article/pii/S2542660524000714>, doi:<https://doi.org/10.1016/j.iot.2024.101129>.
- [12] Hosen, A.S.M.S., Akhter, S., Ra, I.H., 2025. Ensemble learning approaches for multi-class intrusion detection systems for the Internet of Vehicles: A comprehensive survey. *Future Internet* 17, 317.
- [13] Injadat, M., Moubayed, A., Nassif, A.B., Shami, A., 2021. Multi-stage optimized machine learning framework for network intrusion detection. *IEEE Transactions on Network and Service Management* 18, 1803–1816.
- [14] Jha, J., Yadav, J., Naqvi, H., 2025. Milccde: A metaheuristic improved decision-based ensemble framework for intrusion detection in autonomous vehicles, in: *Proceedings of SCIS 2024*, Springer, Singapore.
- [15] Kang, M.J., Kang, J.W., 2016. Intrusion detection system using deep neural network for in-vehicle network security. *PLoS ONE* 11, e0155781.
- [16] Khonde, S.R., Ulagamuthalvi, V., 2025. A secure and efficient deep learning-based intrusion detection framework for the Internet of Vehicles. *Scientific Reports* 15.
- [17] Lokman, S.F., Othman, A.T., Bakar, M.H.A., Razuwan, R., 2018. Stacked sparse autoencoders based outlier discovery for in-vehicle controller area network (CAN). *International Journal of Engineering & Technology* 7, 375–380.
- [18] Neto, E.C.P., Taslimasa, H., Dadkhah, S., Iqbal, S., Xiong, P., Rahman, T., Ghorbani, A.A., 2024. Ciciov2024: Advancing realistic ids approaches against dos and spoofing attack in iov can bus. *Internet of Things* 26, 101209. URL: <https://www.sciencedirect.com/science/article/pii/S2542660524001501>, doi:<https://doi.org/10.1016/j.iot.2024.101209>.
- [19] Nguyen, T.T., Reddi, V.J., 2018. Deep reinforcement learning for cyber security. *IEEE Transactions on Neural Networks and Learning Systems* 29, 2392–2405.
- [20] Nie, L., Ning, Z., Wang, X., Hu, X., Cheng, J., Li, Y., 2020. Data driven intrusion detection for intelligent internet of vehicles: A deep convolutional neural network-based method. *IEEE Transactions on Network Science and Engineering* 7, 2219–2230.
- [21] R., A., V., V., Srinivas, N., A., A.M., 2025. An integrated ids for the internet of vehicles using a large language model framework. *Internet of Things* 33, 101666. URL: <https://www.sciencedirect.com/science/article/pii/S2542660525001805>, doi:<https://doi.org/10.1016/j.iot.2025.101666>.
- [22] Uddin, M.A., Chu, N.H., Rafah, R., Barika, M., 2025. A scalable hierarchical intrusion detection system for internet of vehicles. *arXiv preprint arXiv:2505.16215*.
- [23] Ullah, I., Khalil, I., Bai, X., Garg, S., Kaddoum, G., Shamim, M., 2025. An ensemble-based hybrid model for the detection of attacks in the internet of vehicular things. *IEEE Transactions on Intelligent Transportation Systems* 26, 17914.
- [24] Wahab, F., Ma, S., Zhao, Y., Shah, A., 2025. An explainable three-way neural network approach for intrusion detection in iot ecosystem. *Internet of Things* 33, 101722.
- [25] Wahab, F., Shah, A., Khan, I., Ali, B., Adnan, M., 2024. An sdn-based hybrid-dl-driven cognitive intrusion detection system for iot ecosystem. *Computers and Electrical Engineering* 119, 109545.
- [26] bai ZHAN, H., 2025. Performance comparison of explainable dqn and ddpq models for cooperative lane change decision-making in multi-intelligent industrial iot vehicles. *Internet of Things* 31, 101552. URL: <https://www.sciencedirect.com/science/article/pii/S2542660525000654>, doi:<https://doi.org/10.1016/j.iot.2025.101552>.
- [27] Zhang, C., Shan, G., Roh, B.H., 2024. Fair federated learning for multi-task 6g nwdaf network anomaly detection. *IEEE Transactions on Intelligent Transportation Systems* doi:10.1109/TITS.2024.3461679. early Access.
- [28] Zhang, Y., Li, P., Wang, X., 2019. Intrusion detection for iot based on improved genetic algorithm and deep belief network. *IEEE Access* 7, 31711–31722.
- [29] Zhu, L., Tan, L., 2024. Task offloading scheme of vehicular cloud edge computing based on digital twin and improved a3c. *Internet of Things* 26, 101192. URL: <https://www.sciencedirect.com/science/article/pii/S2542660524001331>, doi:<https://doi.org/10.1016/j.iot.2024.101192>.